Available online at www.sciencedirect.com

ScienceDirect

journal homepage: www.elsevier.com/locate/he

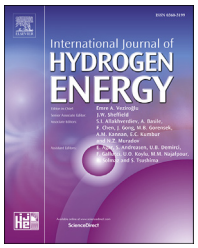

Hierarchically self-assembled ZnO architectures: Establishing light trapping networks for effective photoelectrochemical water splitting

Tian-Feng Hou [a], *Ramireddy Boppella* [b], *Arunkumar Shanmugasundaram* [a], *Dong Ha Kim* [b,**], *Dong-Weon Lee* [a,*]

[a] *MEMS and Nanotechnology Laboratory, School of Mechanical Engineering, Chonnam National University, Gwangju 61186, Republic of Korea*

[b] *Department of Chemistry and Nano Science, Division of Molecular and Life Sciences, College of Natural Sciences, Ewha Womans University, Seoul 03760, Republic of Korea*

ARTICLE INFO

Article history:
Received 19 February 2017
Received in revised form
1 April 2017
Accepted 17 April 2017
Available online 17 May 2017

Keywords:
ZnO hierarchical architectures
Hydrothermal synthesis
Photoelectrochemical water splitting
Light trapping

ABSTRACT

Here we develop photoanodes based on hierarchical zinc oxide (ZnO) nanostructures such as vertically aligned nanorods (NR), nanorods interconnected by thin nanosheets (NR@TN) and nanorods interconnected by dense nanosheets (NR@DN). The morphological variations were successfully controlled by secondary growth time and the plausible formation mechanisms of these hierarchical ZnO architectures were explained based on the experiment analysis. Under simulated light illumination (AM 1.5, 100 mW cm^{-2}), NR@TN produced a photocurrent density of 0.62 mA/cm^2 at 1.23 V vs. reversible hydrogen electrode (vs. RHE). Importantly, 35% enrichment in photoconversion efficiency was observed for NR@TN at much lower bias potential (0.77 V vs. RHE) compared with NR (0.135%) and NR@DN (0.13% at 0.82 V vs. RHE). Key to the improved performance is believed to be synergetic effects of excellent light-trapping characteristics and the large surface-to-volume ratios due to the nanosheet structures. The nanorod connected with thin nanosheet structures improved the efficiency by means of improved charge transfer across the nanostructure/electrolyte interfaces, and efficient charge transport within the material. We believe that the hierarchical ZnO structures can be used in conjunction with doping and/or sensitization to promote the photoelectrochemical (PEC) performance. Further, the ZnO nanorod interconnected with nanosheets morphology presented in this article is extendable to other metal oxide semiconductors to establish a universal protocol for the development of high performance photoanodes in the field of PEC water splitting.

Introduction

Non-renewable fossil fuels such as fuel gas, natural gas, coal and petroleum, have been used as the major energy source in our life throughout the history. As time goes by, the limited storage of fossil-fuel has been incontinently consumed. As a result, the severe energy crisis has become the main problem that should be solved urgently. According to the statistics, the

* *Corresponding author.*
** *Corresponding author.*
E-mail addresses: dhkim@ewha.ac.kr (D.H. Kim), mems@jnu.ac.kr (D.-W. Lee).

http://dx.doi.org/10.1016/j.ijhydene.2017.04.121

solar energy irradiating on the surface of the Earth (1.3×10^5 TW) far surpasses the current global human energy consumption (1.6×10^1 TW in 2010) by roughly four orders of magnitude [1]. Hence, the efficient utilization of solar energy is a promising method to mitigate the energy issues. PEC hydrogen generation, a typical solar energy conversion into chemical energy via photocatalytic water splitting, has attracted considerable attention as it produces the clean hydrogen as a dense fuel.

Since the first demonstration of water splitting by Fujishima and Honda by using TiO_2 photoanode [2], several kinds of metal oxides based photoanodes have been developed and efficiently demonstrated [3–10]. Among them, ZnO has received a great attention due to its high electron mobility [11]. However, the efficiency of ZnO based photoanode has met limited success because of its high recombination rate of e–h (electron–hole) pairs and poor catalytic activity [12,13]. Over the years, several research efforts have been devoted to explore the effective methods to address those drawbacks. Such attempts have been employed through various approaches, such as doping, heterostructure, dye sensitization, quantum dot sensitization and co-catalysts modification.

The best and most widely accepted method to improve the optical absorption, charge-transport path, e–h pair separation, electronic conductivity and surface catalytic activity is the basic structure optimization. Several one dimensional (1D) nanostructures have been widely used to improve the PEC performance of ZnO, such as quantum dot monolayer sensitized nanowire arrays [14–16], core-shelled nanowires [17–19], doped nanorods [20,21] and heterostructure based on nanorods/nanowires [22–24]. The 1D structures can successfully decouple the effective minority-carrier diffusion length (L_{min}) from the penetration depth of the light due to the enhancement of light absorption along the longitudinal wire axis while photogenerated carrier collection occurs along the radial axis [25]. The two dimensional (2D) structures such as planner surface, porous plate, and three dimensional (3D) structures like branched nanowire [26], caterpillar-like nanostructure [27], nanotetrapod [9], textured porous plate [28] and inverse opal structure [29] also have been gained great attention. The 3D structures show the improved PEC performance comparing to the 1D and 2D materials due to its higher light harvesting efficiency [30–32]. Recently, the hierarchical structure received great attention for water splitting due to the high surface area which increases the interface area between the electrolyte and photoanodes. However, the arrangement of the microstructure is also crucial. The vertically aligned hierarchical-branched structure branched structure [26] has much higher photocurrent density than randomly distributed branched structure [27]. But the drawback of the hierarchical architectures is a mass of recombination sites for e–h pair which leads to weaken the PEC performance. As shown in Table 1, the PEC performance of pure ZnO largely changes with its different structures.

As discussed in the preceding section, each structure has its own intrinsic advantages and disadvantages. The excellent hydrogen evolution ability can be obtained with reasonable combination of these structures. The crystal structure of zinc oxide consists of thermodynamically stable polar-terminated ±001 and non-polar low symmetry ±100 crystallographic faces. In general low-symmetry non-polar faces are more stable than the polar face, leading to the fast crystal growth of zinc oxide along *C*-axis (⟨0001⟩ direction) [33]. As a result several 1D nanostructures with exposed crystal facets of (100) and (110) are usually obtained [34]. Due to the inherent high surface energy of ±001 polar planes and the related thermodynamic restriction, controlling the morphology of zinc oxide through the wet-chemical synthesis route remains an important challenge for the materials scientists.

Table 1 – PEC performance of ZnO photoelectrodes.

Structure	Photocurrent density (mA/cm^{-2})	Ref.
Branched ZnO NWAs (B–ZnO)	0.75, 1.4 V (vs. RHE)	[26]
Pillar ZnO NWAs (P–ZnO)	0.60, 1.4 V (vs. RHE)	
"Caterpillar-like" branched ZnO nanofibers (BZNs)	0.52, 1.2 V (vs. RHE)	[27]
Vertically-aligned NWs	0.35, 1.2 V (vs. RHE)	
ZnO nanorod	0.33, 1.0 V (vs. Ag/AgCl)	[23]
N-doping branched ZnO nanotetrapods	1.70, 1.2 V (vs. Ag/AgCl)	[9]
Branched ZnO nanotetrapods	0.30, 1.2 V (vs. Ag/AgCl)	
ZnO@InP QD-mix	1.20, 1.0 V (vs. Ag/AgCl)	[14]
ZnO NWAs	0.60, 1.0 V (vs. Ag/AgCl)	
ZnO nanostructure thin film	0.093, 1.23 V (vs. Ag/AgCl)	[48]
N doped ZnO NRAs	0.16, 1.1 V (vs. SCE)	[20]
Textured porous ZnO plates	0.40, 1.2 V (vs. RHE)	[28]
CdSe/ZnO textured porous film	3.10, 1.2 V (vs. RHE)	
NR	0.5, 1.23 V (vs. RHE).	Present work
NR@TN	0.62, 1.23 V (vs. RHE)	
NR@DN	0.45, 1.23 V (vs. RHE)	

Over the years, considerable efforts have been devoted for selectively passivating the axial growth by using suitable structure directing agents. The several organic additives, such as ethylene glycol, ethylenediamine, dodecyl sulphate, poly (vinyl alcohol), etc. have been successfully used to control the size and shape of zinc oxide nanocrystals. In continuation of these great efforts, herein, we report an ethanolamine assisted hydrothermal synthesis route to prepare ZnO nanorod hierarchical nanostructure. The several ZnO nanostructures such as (i) nanorods (NR), (ii) nanorods interconnected by thin nanosheets (NR@TN) and (iii) nanorods interconnected by dense nanosheets (NR@DN) were prepared by controlling the secondary growth time. Finally, the fabricated ZnO photoanodes were used for the PEC water splitting under solar light illumination. All the ZnO photoanodes show excellent photocurrent density, among them NR@TN shows the maximum photocurrent density of 0.62 mA/cm^2 at 1.23 V (vs. RHE), whereas the photocurrent density of NR and NR@DN is found to be 0.5 mA/cm^2 and 0.45 mA/cm^2 at 1.23 V (vs. RHE), respectively. The NR@TN not only possesses the intrinsic

advantages of vertically aligned 1D nanostructure, but also possesses excellent charge transfer ascribed to the thin nanosheets. The excellent PEC performance, highest light absorbance and lowest charge transfer resistance of the NR@TN are attributed to the excellent ability of decoupling photogenerated minority-carrier diffusion length from light-absorption length and multi-reflection of nanorods arrays (NRAs) along with effective transfer of photons by thin nanosheets. Thus, the architecture of nanorods interconnected by thin nanosheets is an effective structure for PEC water splitting.

Experiment

Materials

Zinc acetate dihydrate ($Zn(CH_3COO)_2.2H_2O$), ethanolamine ($NH_2CH_2CH_2OH$) and sodium hydroxide (NaOH) were purchased from Sigma–Aldrich. All the chemicals are analytical reagent (AR) grade and used without any further purification. Deionized water (18.2 MΩ at RT) was used throughout the experiment process.

Preparation of ZnO nanostructures

ZnO films were prepared based on a two-step seed-layer-mediated hydrothermal method. The fluorine-doped tin oxide (FTO) with a sheet resistance of 7 Ω/sq was (1.5×2 cm^2) used as the substrate to prepare the film. First the FTO substrate was cleaned via ultrasonication by sequentially immersing into isopropenyl acetylene, acetone, and deionized water for 15 min, respectively. Seed layer solution was prepared with addition of 1 mmol (~0.220 g) of zinc acetate dihydrate in 50 mL of water followed by the addition of 4 mmol (~0.160 g) sodium hydroxide under constant magnetic stirring. The cleaned FTO substrates were put into the seed solution for 4 h at the temperature of 75 °C followed by drying at 150 °C for 30 min in the oven.

The ZnO nanostructures were grown on the seed layer with typical hydrothermal method. In a synthesis procedure 2 mmol (0.595 g) of zinc nitrate dissolved in 30 mL of deionized water followed by the drop by drop addition of 2.5 mL of ethanolamine. After 15 min of constant magnetic stirring the solution was transferred to the Teflon-lined autoclave then the seeded FTO substrates were placed face-down with 45° against the wall. Then hydrothermal reaction was performed at 150 °C for reaction time of 12 h, 18 h and 24 h to obtain desired structures. After that, the films were taken out and washed with deionized water and calcined at 400 °C for 4 h with heating rate of 3 min/°C and cool down to room temperature naturally.

Characterizations

The PEC performance measurement was carried out according to the method published by Chen et al. [35]. A standard three-electrode electrochemical cell with a Pt wire counter electrode and an Ag/AgCl reference electrode was used for all of the PEC measurement. The electrolyte was 0.5 M Na_2SO_4 aqueous solution (with pH buffered to ~7.0) which had been bubbled with N_2 flow for 1 h to exclude the dissolved oxygen. The working electrodes were illuminated from the FTO side with a simulated sunlight from a 300 W Xe lamp equipped with an AM 1.5G filter. Conductive silver paste was painted on the top of the electrode. The calibration was performed using an NREL-certified silicon photodiode equipped with a KG-5 filter. The potentials were measured vs. the Ag/AgCl reference electrode and were converted to the reversible hydrogen electrode (RHE) scale using the Nernst function:

$$E_{RHE} = E_{Ag/AgCl} + E^0_{Ag/AgCl} + 0.059pH$$

E_{RHE} is the converted potential vs. RHE. $E_{Ag/AgCl}$ is the external potential measured against the Ag/AgCl reference electrode. $E^0_{Ag/AgCl}$ is the standard electrode potential of Ag/AgCl reference electrode (0.1976 V vs. RHE at 25 °C). The charge transfer and transport efficiencies were estimated by measuring the photocurrent in 0.5 M Na_2SO_4 + 0.5 M Na_2SO_3 aqueous solution as functions of applied potential under AM 1.5G simulated solar light illumination. The key assumption for this method is that the oxidation kinetics of Na_2SO_3 is very fast and its charge transfer efficiency is 100%, so the ratio of photocurrent density measured in Na_2SO_4 and Na_2SO_3 gives the charge transfer efficiency (η transfer) for Na_2SO_4.

$$\eta \text{ transfer} = J(Na_2SO_4)/J(Na_2SO_3)$$

The incident photon-to-current conversion efficiency (IPCE) was measured in the wavelength range of 300–600 nm at a potential of 1 V (vs. RHE) using a system including an illumination source with a monochromator (McScience with a 300 W xenon light source) and a set of filters for order sorting. The transmittance (T, %) and reflectance (R, %) of NR, NR@TN and NR@DN were studied using a Varian 5000 UV–vis–NIR spectrophotometer. For the reflectance measurement, the samples were mounted at the backside of the integrating sphere and the reflectance spectra were normalized to the reflection of a white-standard. The transmittance spectra were obtained by comparing the transmittance of test samples with a calibrated Si reference photodiode. The absorption plus scattering was calculated from these measurements with the formula $A + S = 100 - T - R$ (A is the absorption, S is the scattered light that was not accounted for in the measurement, T is the total transmittance, and R is the total reflectance). Relative electrochemical surface area was determined through double-layer capacitance measurements by cyclic voltammetry in the region between −0.55 and −0.35 V vs. Ag/AgCl in 0.5 M Na_2SO_4 + Na_2SO_3 under dark. The scan rate varied from 25 to 300 mV/s was applied. The morphology was observed through the field-emission scanning electron microscopy (FE-SEM, Phillips XL30S) operating at 15 kV and transmission electron microscopy (TEM, HR-TEM, JEM-2100F, JEOL). The crystalline structure, phase purity and composition of the as-synthesized material were elucidated with an X-ray powder diffraction (XRD, Rigaku) operating at 40 kV and 40 mA with the speed of 4°/min. The molecular structure of the as-prepared material was analyzed with a laser Raman spectrophotometer (NRS-5100, JASCO). The electronic state of the material was characterized with X-ray photoelectron spectroscopy (XPS), in which

ESCALAB-MKII with Al Kα X-ray ($h\nu$ = 1486.6 eV) as the emission source.

Results and discussions

Morphological evaluations of the primary and secondary growth of the ZnO nanostructures were characterized by using electron microscopy in both scanning and transmission mode along with selected area electron diffraction and high resolutions transmission electron microscopy. Fig. 1(a–i) shows the FESEM images of the as prepared ZnO architecture arrays grown on the FTO substrate with different hydrothermal reaction time.

The vertically aligned ZnO nanorods were obtained when the reaction time maintained at 12 h (Fig. 1(a–c)). The panoramic observation (Fig. 1a) discloses the numerous nanorods with uniform shape and size. The higher magnified image (Fig. 1b) clearly shows the well aligned nanorods of size ~100 nm and the tips of the each nanorod was connected with very thin nanosheets indicating that the secondary crystal growth with nanosheets morphology takes place during the hydrothermal reaction time. As observed from TEM microscopy analysis (Fig. 2(a–c)), the nanosheets grown along the backbone of the nanorods and the crystal growth of nanosheets take place perpendicular direction to the vertically aligned nanorods. The nanorods interconnected by thin nanosheets (Fig. 1(d–f)) were obtained when the reaction time increased to 18 h. As seen from the TEM analysis (Fig. 2(e–g)), half length of the nanorods which size are ~100–150 nm and were covered by the thin nanosheets. Further increasing the hydrothermal reaction up to 24 h, the nanosheets became much denser and covered the whole of the nanorods from tip to root (Fig. 1(g–i) and Fig. 2(i–k)). After the secondary growth, the ZnO nanorods surface became rough and bumpy due to the secondary grown 2-dimensional ZnO nanosheets. The high-resolution TEM (HRTEM) in Fig. 2(d,h,i) shows clear two-dimensional lattice fringes of the individual ZnO nanorods, which further confirm that the nanorods are well crystalline. It can be clearly seen from the HRTEM analysis that the ZnO (001) fringes perpendicular to the rod axis are separated by 0.28 nm on average, indicating crystalline ZnO nanorod growth along the ZnO [001] direction. Selected area electron diffraction patterns show Laue spots along with the diffraction rings, indicating very good crystallinity of the synthesized material (inset: Fig. 2).

A series of controlled experiments with different hydrothermal reaction time were carried out to explore the ZnO nanosheets secondary growth formation mechanism. The different stages of formation for nanosheets interconnected nanorods were captured in a time dependent analysis that provided important clues toward to determine the formation mechanism. The hydrothermal reaction was arrested at different time intervals and the intermediate products were collected and characterized concomitantly using electron microscopy analysis. The products obtained at 14 h and 16 h hydrothermal reaction time were shown in Fig. S1. Nanorods were interconnected by the thin nanosheets, which was obviously observed after growing 14 h and 16 h. As observed from the products acquired at different hydrothermal reaction time, the nanosheets became thicker and thicker comparing to the secondary growth time of 12 h. It is well consistent with the previous speculation which advocates that the nanosheets gradually grow and completely cover nanorods and the

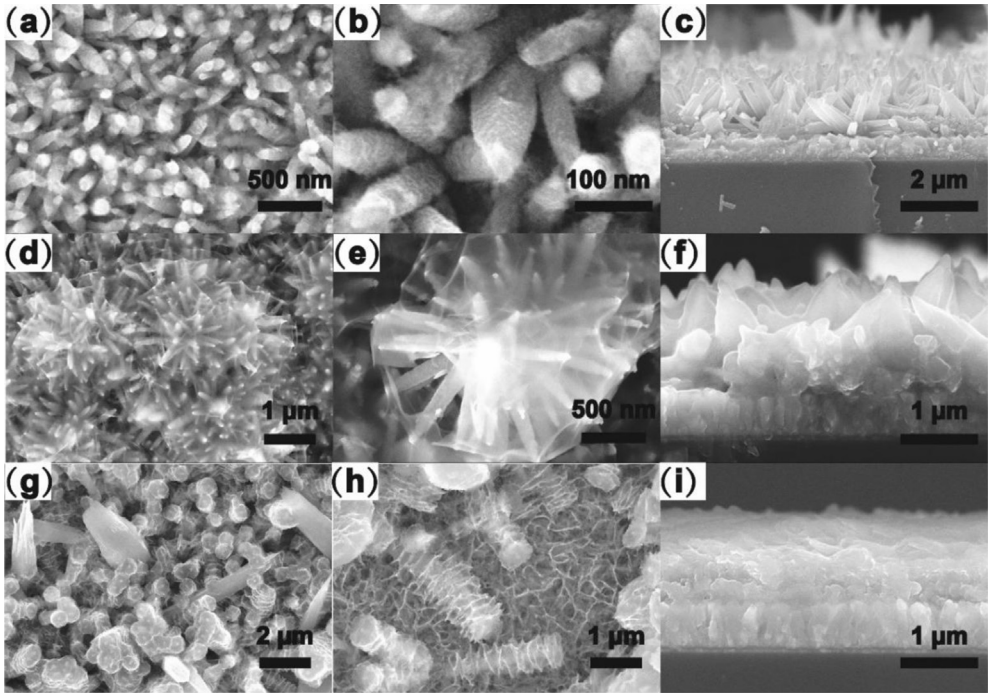

Fig. 1 – (a–i) Morphological evaluations of the as prepared materials in scanning electron microscopy mode at different magnifications; (a–c) nanorods (NR); (d–f) nanorods interconnected by thin nanosheets (NR@TN); (g–i) Nanorods interconnected by dense nanosheets (NR@DN).

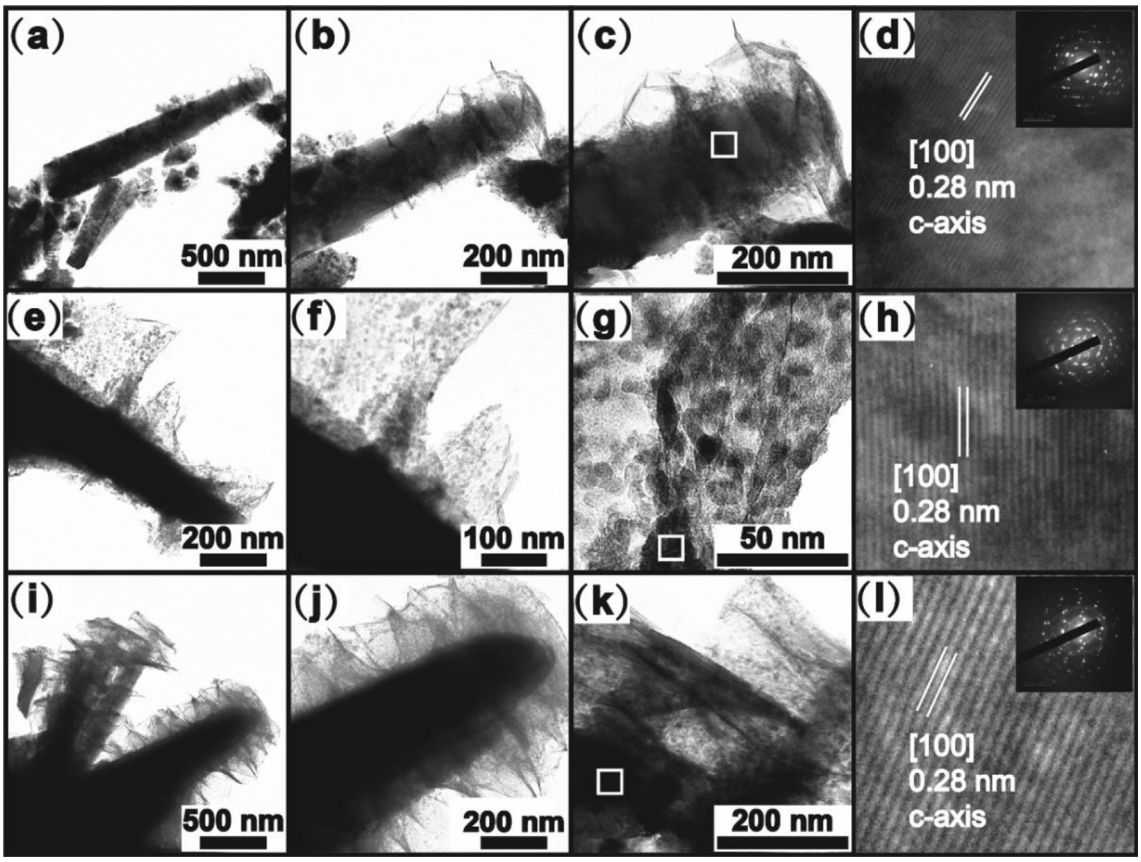

Fig. 2 – (a–l) Morphological evaluations of the as prepared materials in transmission electron microscopy mode at different magnifications; (a–c) nanorods (NR) and (d) corresponding HRTEM and SAED pattern; (e–g) nanorods interconnected by thin nanosheets (NR@TN) and (h) corresponding HRTEM and SAED pattern; (i–k) Nanorods interconnected by dense nanosheets (NR@DN) and (l) corresponding HRTEM and SAED pattern. The corresponding area of HRTEM was denoted by a rectangle for each sample.

nanosheets become denser and denser with the increasing secondary growth time.

As evidenced from the electron microscopy analysis the growth mechanism of the nanosheets is strongly dependent on the hydrothermal reaction time. In general, the low-symmetry non-polar faces are more stable than the polar face, leading to the fast crystal growth of zinc oxide along C-axis (⟨0001⟩ direction). However, the anisotropic growth of the crystal along the ⟨0001⟩ direction also exists due to the inherent asymmetry along the c axis [33]. In secondary process, the electro positively charged, Zn-terminated ZnO (001) top plane favours the chemisorptions of the negatively charged amine ions, suppressing the C-axis growth of the ZnO but causing growth on the non-polar ZnO side-planes [36]. Under these reaction conditions, with the time increasing, the secondary nucleation sites were introduced on the surface of the ZnO nanorods [37], the nanorods stop growing, nucleation and secondary grown on the accommodation sites on the tip of ZnO nanorods was observed. With the randomly oriented crystals grew further, the grown structure began to impinge on other neighbouring crystal and preferred to grown as nanosheets [37]. Further prolonging the hydrothermal reaction time, the nucleation sites were spread from tip to root of nanorods, and nanosheets were became more and more dense to fill the interspace between nanorods. As evidenced from the cross-sectional view of electron microscopy images there are no significant changes in the film thickness but the nanosheets became much dense and denser during the secondary growth time (Fig. 1(c, f, i)).

The crystal structures of the as prepared materials were characterized by the powder X-ray diffraction analysis. Because the thickness of the as prepared ZnO films is very thin, obvious tin oxide diffraction patterns along with ZnO were shown in the XRD pattern, which can be certificated by the ZnO film synthesized with secondary growth time of 18 h. To well study the crystal structure of as prepared films, films were scratched from the FTO substrate. The obtained diffraction patterns (Fig. 3a) can be perfectly indexed to the hexagonal wurtzite crystal structured zinc oxide and the calculated lattice parameters are exactly matched well with the ZnO (JCPDS card no. 36-1451). The sharp and strong diffraction patterns indicate that the ZnO nanoarchitectures possess high crystalline nature, and no other diffraction patterns were detected which indicates the high purity of the sample. The average crystalline size of the material is calculated by using Scherrer's equation [38]. Calculated crystalline size of NR, NR@TN and NR@DN is ~22.1, 22.7 and 22.9 nm, respectively.

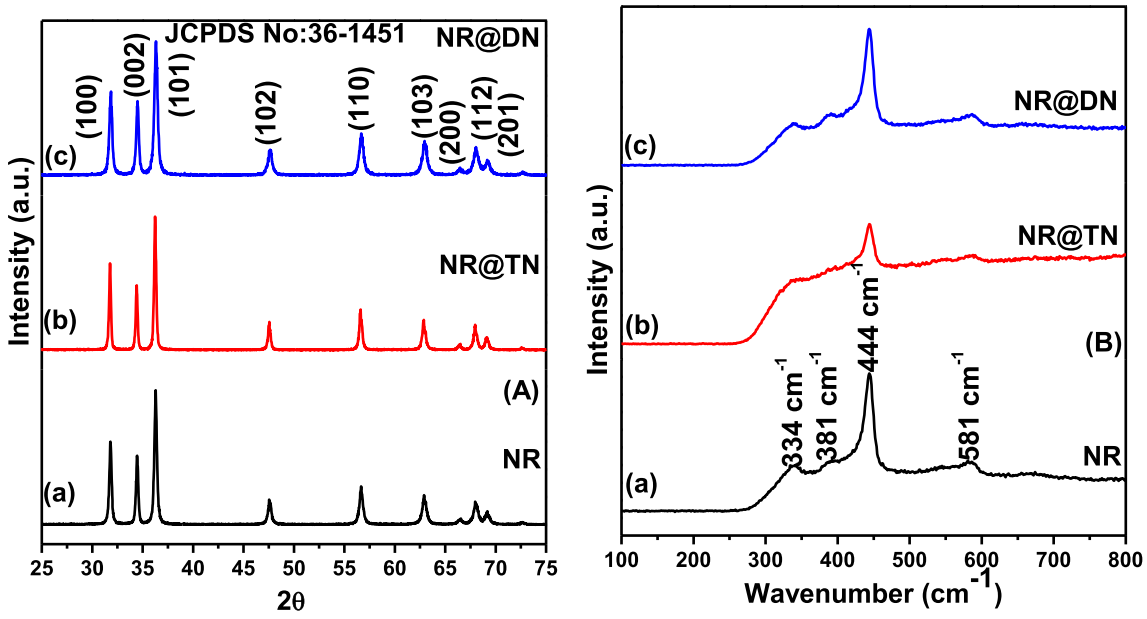

Fig. 3 – (A) The X-ray diffraction pattern and (B) Raman spectroscopy analysis of as prepared ZnO nanostructures. (a) Nanorods (NR), (b) nanorods interconnected by thin nanosheets (NR@TN), (c) nanorods interconnected by dense nanosheets (NR@TN).

The phase purity and crystal structure of the as prepared zinc oxide nanostructures were further characterised by the Micro-Raman spectroscopy analysis (Fig. 3b). There were four phonon modes of Raman scattering in different configurations, which correspond to 334 cm^{-1}, 381 cm^{-1}, 444 cm^{-1}, 581 cm^{-1}, respectively. Specifically, these four modes are indexed to the second order or multiple-phonon mode of E_2 (high) – E_2 (low) scattering arising due to the overtones or combination of first order modes, the first order Raman scattering corresponding to A_1 (TO) phonon mode, the E_2 (high), and the A_1 (LO) phonon mode which is associated with presence of oxygen vacancies, respectively. This result is well consistent with the ZnO Raman spectroscopy study carried out by Schumm [39]. The obtained Raman modes further confirm that the wurtzite crystal structure of zinc oxide and the analysis are well agreed with the XRD analysis.

The chemical states and chemical composition of the ZnO films of NR, NR@TN and NR@DN were further studied by XPS analysis. The peak positions were calibrated with C_{1s} at 284.6 eV and the typical survey XPS spectrums reveal (Fig. S3) that the as-prepared ZnO films consist of photoelectron peaks of Zn, O, and C. In addition, Auger peaks of Zn (LMM) and O (KLL) were also observed in the XPS spectrum. Fig. 4(I) shows the core level spectra of zinc oxide in Zn region. The high resolution spectra show the two obviously symmetric peaks with little difference binding energy. The peaks at 1021.8 ± 0.1 eV and 1044.9 ± 0.1 eV are affiliated to $Zn_{2p3/2}$ and $Zn_{2p1/2}$, respectively. This evidently illustrates that the chemical valence of Zn at the surface of all films is +2 oxidation state in zinc oxide [22,40]. Slight difference of the binding energy is probably due to the little different morphologies of ZnO nanostructures which possess different amount of nanosheets and different size of nanorods. This viewpoint can be proved from the study of Al-Gaashani et al., where the author stated that the chemical environment interaction with the surface atoms (composition of the 5 nm top thickness of the surface) and the variation of the texture coefficients with morphology are the main reasons for the binding energies difference [40]. The core level spectra of oxygen in O1s region (Fig. 4II) were deconvoluted into four peaks. The peaks posited at 529.9 eV (O1) are ascribed to the O^{2-} ion in the wurzite structure, which are encompassed by the Zn atoms with their full complement of nearest-neighbour O^{2-} ions; the peaks at 531.05 ± 0.1 eV (O2) are associated to the existence of OH bonds, i.e. ZnO (OH); and the binding energy peaks at 532.15 ± 0.1 eV (O3) are attributed to the specific chemisorbed oxygen. The peak located at 528.2 ± 0.05 eV (O4) with a lowest intensity, which is ascribed to the oxygen from an ZnO $(1\,0\,\bar{1}\,0)$ surface [41].

The optical properties of the ZnO NR, NR@TN and NR@DN were investigated using UV–vis spectrophotometer to distinguish their light absorption features. The light harvesting efficiency was calculated by subtracting transmittance (T, %) and reflectance (R, %) from 100% incident light. The reflectance spectra (Fig. 5a) and the transmittance spectra (Fig. 5b) clearly demonstrate that the different optical properties were observed when exciting photon energy is smaller than the band gap energy of ZnO (λ > ~400 nm). The optical reflectance of the all samples sharply decreases at a wavelength range shorter than 360 nm due to the strong intrinsic light absorption of ZnO, which corresponds to the band gap in the absorption spectrum since it demonstrates the least amount of energy required for a photon to eject an electron from valance band to conduct band [35]. The reflectance at λ > 450 nm of the NR@DN is higher than the NR and NR@TN (Fig. 5a), while the NR exhibits the lowest reflectance among the three samples. The NR@DN exhibits the highest reflectance and lowest transmittance in the whole visible spectrum, while NR shows

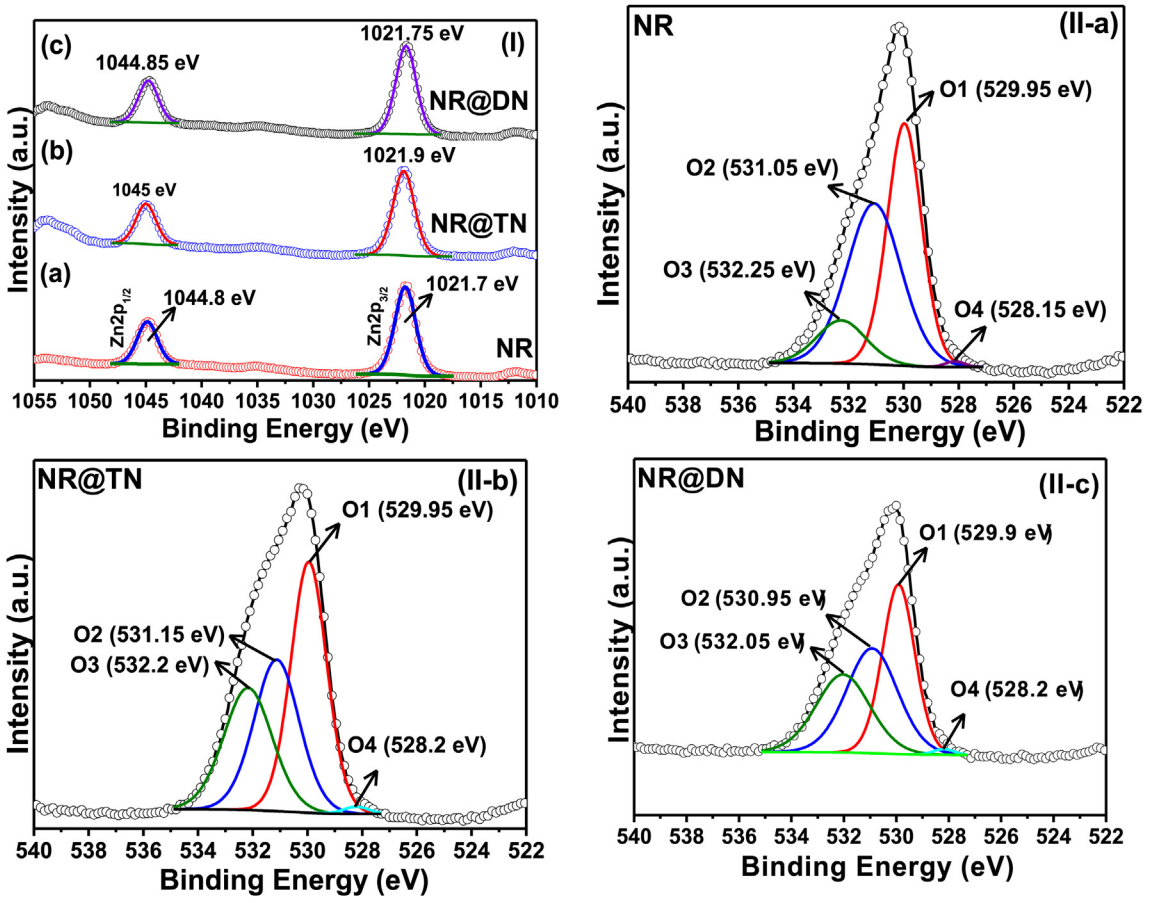

Fig. 4 – The core level X-ray photoelectron spectra of as prepared ZnO nanorods (NR), nanorods interconnected by thin nanosheets (NR@TN), nanorods interconnected by dense nanosheets (NR@TN) in zinc 2p (I) and in oxygen (II (a–c)) region oxygen, where the black lines represent the experimental XPS data, and the green red lines are the background, other colourful lines are the fitting of the experimental data. (For interpretation of the references to colour in this figure legend, the reader is referred to the web version of this article.)

the lowest reflectance and highest transmittance in the almost of the visible range (>450 nm). The strong reflectance of NR@DN is probably due to the full coverage of interconnected dense film along the vertically aligned ZnO NR leads a multiple reflection, thus it exhibits high reflectance in the visible region. These results are in good agreement with the SEM data (Fig. 1) On the other hand, NR exhibits relatively large open space between the adjacent nanorods leads to the only single reflection, thus displays the comparatively lower reflectance in the visible region.

Differing from the NR and NR@DN, NR@TN possesses moderate transmittance and reflectance in the visible region; however, it possesses a higher light absorption in the visible region (Fig. 5c). The multiple reflections among the nanorod interconnected nanosheets, on the one hand, theoretically extend the light absorption path and increase the interaction sites of the ZnO nanostructures with excitation. However, dense nanosheets cannot effectively absorb the photons due to the long transport length between the nanosheets and nanorods so that most of the e–h pairs would be recombined before electrons were transferred through nanorods and holes diffuse to the electrolyte. An appropriate theory of "light trapping" can be used to better explain it, although this perspective has long been used to effectively improve the solar cell performance [42,43]. In the solar cell, structure which consists of a high-index thin-film active layer with a high-reflectivity mirror at the bottom and air on top is always applied to form light trapping, in which the propagation distance along the film is much longer than the thickness of the film [44]. Therefore, in the present work, it is reasonable to attribute the enhanced light absorbance to the formation of light trapping made by the very thin nanosheets which interconnect the nanorods completely, in which the nanorods can be worked as a multi-reflector [45] to make photons transport longer way after they are absorbed by thin nanosheets.

The surface area and pore size distribution of as prepared zinc oxide nanostructures were characterized by N_2 adsorption/desorption isotherm method at 77 K. The adsorption–desorption (Fig. 6a) profile exhibits typical type-IVisotherms hysteresis loops, which indicates that the mesoporous nature of the materials combining with the pore size distribution of 2–50 nm (Fig. 6b). However, there is little difference among the isotherm profiles of NR, NR@TN, and NR@DN, in which the NR and NR@DN exhibit type-IVb due to the hysteresis of desorption instead of type-IVa as that of NR@TN. This indicates that the pore width of NR@TN exceeds

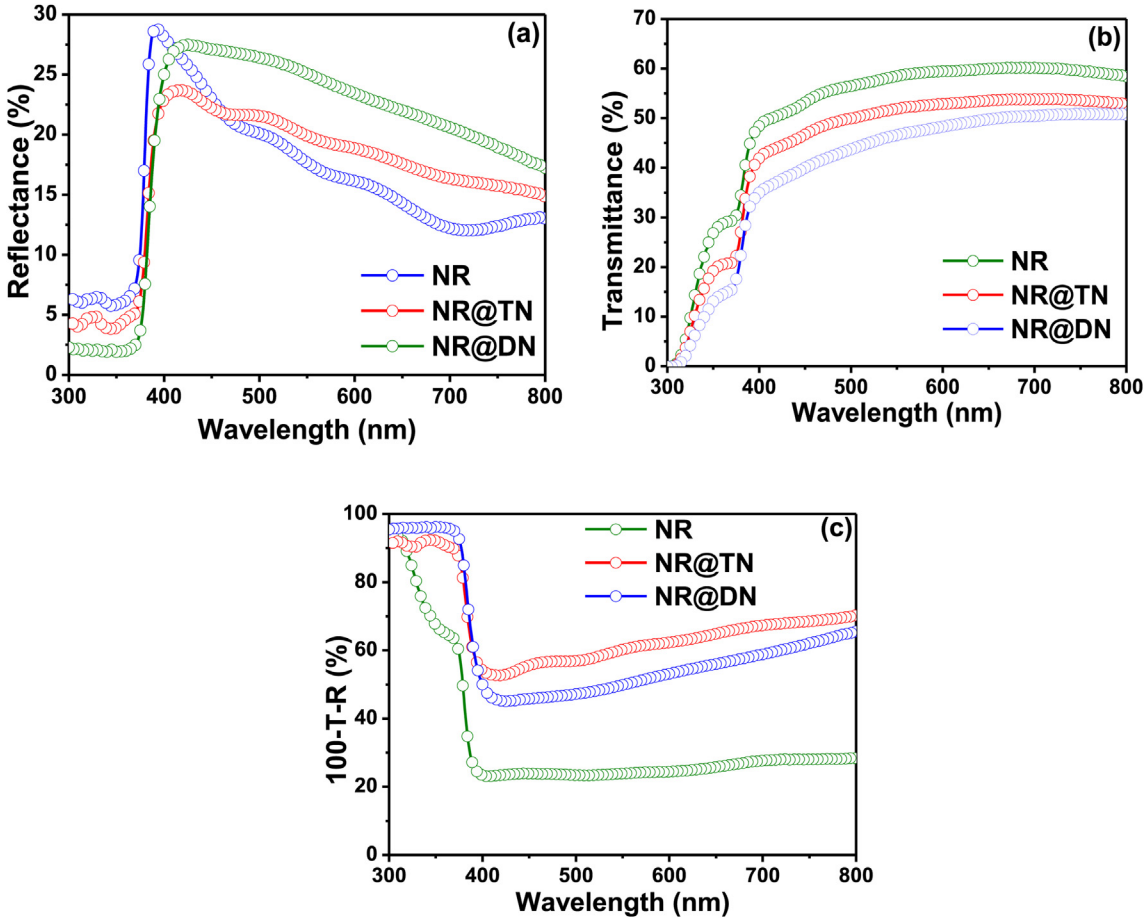

Fig. 5 – The ultra violet diffused reflectance spectroscopy analysis of as prepared ZnO nanorods (NR), nanorods interconnected by thin nanosheets (NR@TN), nanorods interconnected by dense nanosheets (NR@TN) in (a) reflectance mode, (b) transmittance mode and (c) integrated absorption spectra.

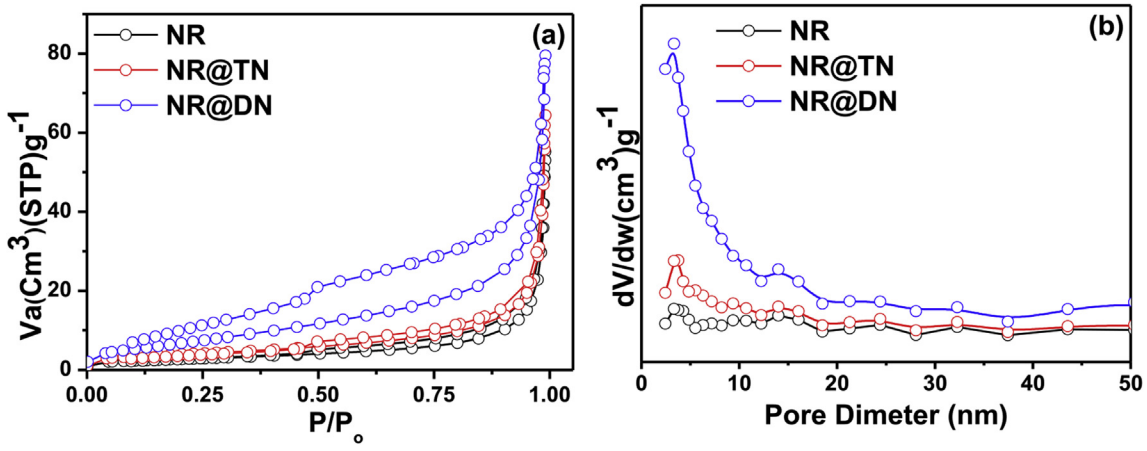

Fig. 6 – (a) Adsorption and desorption isotherms of nitrogen and (b) Barrett–Joyner–Halenda (BJH) pore-size distributions for as prepared ZnO nanorods (NR), nanorods interconnected by thin nanosheets (NR@TN), nanorods interconnected by dense nanosheets (NR@TN).

a certain critical width of ~4 nm [46], in contrast, NR and NR@DN exhibit conical and cylindrical mesopores that are closed at the tapered end with smaller width [47] comparing to the NR@TN.

A sharp "knee" point near P/P_0 is around 0.04–0.046 in the isotherm. This inflection point marks the completion of the first adsorbed monolayer–multilayer adsorption on the mesoporous walls, from where the specific surface area of ZnO

was calculated. The specific surface area of NR, NR@TN and NR@DN is 9.549 m^2/g, 13.93 m^2/g and 22.07 m^2/g, respectively. With the P/P_0 increasing, a sharp increase in the isotherm slope was observed above 0.90, from which the capillary condensation was presented until the pores followed by saturation while the pores were filled with liquid. This high value of P/P_0 indicates that the pore size of ZnO is at the upper mesopore to low macropore range. The pore size distributions of the as-prepared ZnO nanostructures are concentrated on the range of 2.5–5 nm and the NR@DN possesses much more pores than others, which plays a decisive role for the specific surface area.

PEC performance of as fabricated ZnO photoanodes based on NR, NR@TN, NR@DN was investigated. The analyses were quantified through the photocurrent density vs. potential (J–V) measurements (Fig. 7a) under dark and simulated illumination (AM 1.5) in a three-electrode cell configuration. All the fabricated ZnO photoanodes displayed a pronounced photocurrent density upon illumination implying efficient light harvesting and charge separation. To effectively evaluate the ZnO photoanodes, the dark current density measurements were carried out. The measurement shows the stable response (indicated as dotted line in Fig. 7a) and no apparent photocurrent was observed because of no photons penetrated the material. The photocurrent under dark condition can be almost negligible comparing to photo-current generated under illuminations (Fig. 7a). Therefore, it can be used to quantitatively estimate the photocurrent densities obtained under the illumination without subtracted.

The fabricated photoanodes show excellent photo response with increasing bias voltage (0 to +1.8 V) under the illumination. The current densities of all photoanodes rapidly increase when the external applied potential exceeds the onset potential around ~0.3 V (vs. RHE). It is worth mentioning that nanorods interconnected by nanosheets samples possess slightly lower onset potential comparing to the NR structures. Among the three photoanodes, NR@TN demonstrated the best PEC performance with the photocurrent density of 0.62 mA/cm^2 at 1.23 V (vs. RHE) comparing to the photoanodes fabricated by NR and NR@DN. In contrast, the NR@DN showed the lower photocurrent density of 0.47 V (vs. RHE) than the NR (0.5 V (vs. RHE)). The slightly higher photocurrent density and lower onset potential obtained for NR@TN can be ascribed to the enhanced light capturing ability and the increased semiconductor/liquid interfaces which was beneficial for charge transport and chemical reaction. Most importantly, the photocurrent densities are comparable with other pure ZnO photoanodes as shown in Table 1 which summarizes some of the PEC performance data achieved by various ZnO photoelectrodes.

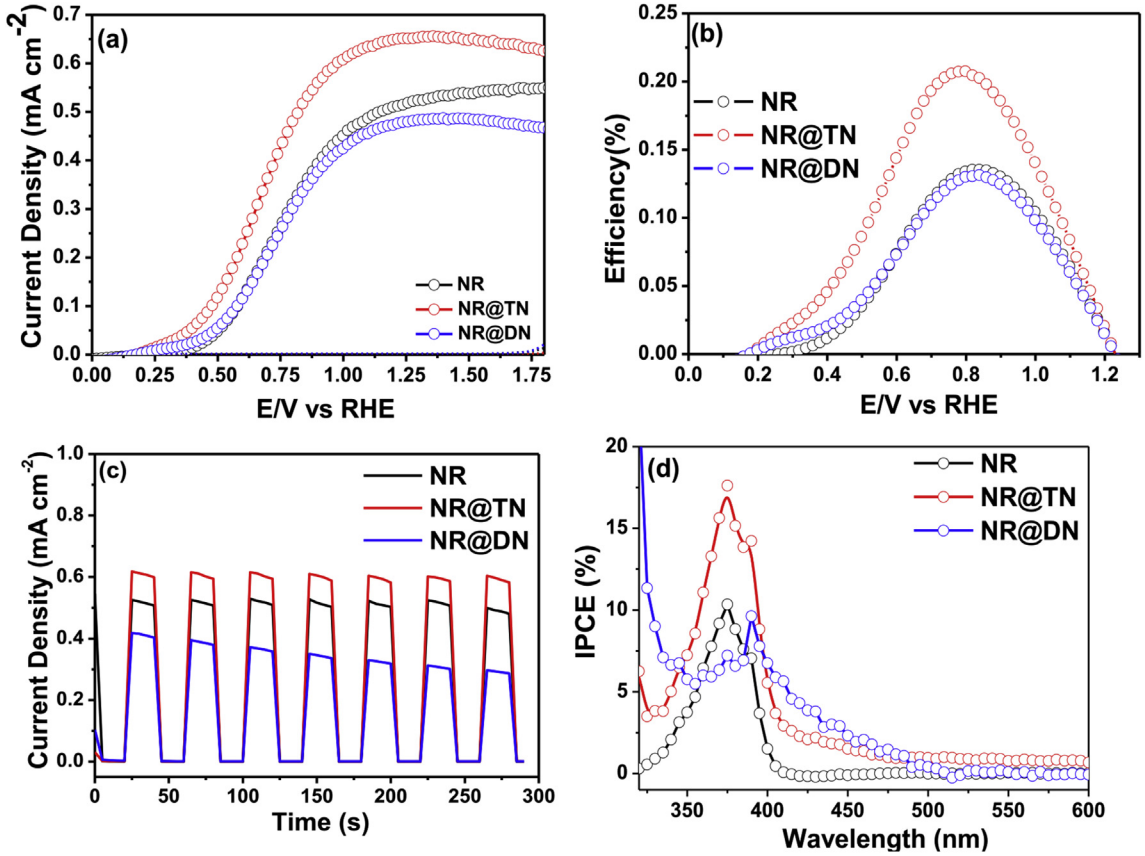

Fig. 7 – (a) J–V curves recorded on the three types of ZnO nanostructures at a scan rate of 10 mV s^{-1} under 1 sun illumination (100 mW cm^{-2} AM 1.5G), dark current is showed in dotted line, (b) Photoconversion efficiency (η) of the three types of ZnO nanostructures as a function of applied potential referenced to RHE, (c) Chronoamperometric I–t curves under chopped illumination at 1.23 V (vs. RHE) and (d) IPCE spectra of nanorods (NR), nanorods interconnected by thin nanosheets (NR@TN) and nanorods interconnected by dense nanosheets (NR@DN).

The photoconversion efficiency of all photoanodes was calculated based on the equation, $\eta = I\ (1.23 - V_{app})/J_{light}$, where V_{app} is the applied voltage vs. reversible RHE, I is the photocurrent density at the measured potential, and J_{light} is the irradiance intensity of 100 mW cm^{-2} (AM 1.5G). Fig. 7b shows the calculated photoconversion efficiencies as a function of external potential vs. RHE. The NR and NR@DN samples exhibit an optimal photoconversion efficiency of 0.135% and 0.13% at 0.82 V (vs. RHE), respectively. Whereas the photoconversion efficiency of NR@TN photoanode is ~0.2% even at lower potential of 0.77 V (vs. RHE). The efficiency of NR@TN photoanode is almost 35% higher than that of photoanodes based on NR and NR@DN.

To examine the instant photo response for the photoanodes, current density vs. potential (J–V) measurements under chopped light illumination (Fig. 7c) were obtained. One can clearly observe the steep increase of transient photocurrents when light illumination was turned on, whereas photocurrents were suddenly decreased when light illumination was turned off. As seen from Fig. 7c, the photocurrent density of photoanodes based on NR and NR@TN shows no photocurrent deactivation. However, in the case of NR@DN photocurrent deactivation is observed. It could be explained based on the following lines: at the initial stage of reaction the generated electrons rapidly transferred to the conduction band, however, with the time increase, electrons would tend to recombine with holes on the NR@DN surface due to its high recombination sites. The observed changes further supported through the electrochemical impedance spectroscopy (EIS) (Fig. 8a) and charge transfer efficiency analysis in the following sections.

To further investigate the light harvesting efficiency of fabricated ZnO photoanodes at different wavelength, incident-photon-to current conversion efficiency (IPCE) analysis was carried out from 300 to 600 nm wavelength under 1 V (vs. RHE) bias. IPCE is an effective parameter to characterize the light harvesting efficiency of different photoanodes because it is independent from the light sources so that the photocurrent can be collected per incident photon flux as a function of the incident light wavelength. The IPCE can be calculated by the following equation [35]:

$$\mathrm{IPCE}(\lambda) = \mathrm{EQE}(\lambda) = \frac{\mathrm{electrons/cm^2/s}}{\mathrm{photons/cm^2/s}} = \frac{\left|j_{ph}\ (\mathrm{mA/cm^2})\right| \times 1239.8\ (\mathrm{V \times nm})}{P_{mono}\ (\mathrm{mW/cm^2}) \times \lambda\ (\mathrm{nm})}$$

where j_{ph} is the measured photocurrent density at a specific wavelength, the 1239.8 (V × nm) represents a multiplication of h (Planck's constant) and c (the speed of light), P_{mono} is the calibrated and monochromatic illumination power intensity in mW cm^{-2}, and λ (nm) is the wavelength at which this illumination power is measured.

As observed from the IPCE analysis (Fig. 7d) the ZnO photoanodes show the strong photoactivity in UV region from 300 to 400 nm. The NR@TN exhibited a noticeable improvement in the IPCE value with comparing to other two photoanodes based on NR and NR@DN in the inter band transition absorption region of ZnO. The enhanced IPCE in the UV region could be ascribed to the prolonged lifetime of photogenerated charge carriers. It is interesting to note that nanorod interconnected to the nanosheets samples (NR@TN and NR@DN) showed significant absorption in the visible region (420–470 nm); the absorption is more pronounced for the NR@DN structures in the visible region. The results are corroborated with the observed absorption spectra (Fig. 5c).

The EIS was carried out to investigate the charge transport properties of as-prepared photoelectrodes (Fig. 8). The radius of the semicircle arcs in the Nyquist plot relates to the charge transfer resistance (R_{ct}) of electrode and a smaller radius indicates the faster charge transfer properties [49] in the system. As can be seen from Fig. 8a, NR@DN photoanode showed the largest semicircle arcs, whereas NR@TN showed the smallest semicircle arcs which is much lower than other two. In addition, slightly large charge transfer resistance was observed for NR than NR@TN. The same charge transfer phenomenon was also observed in the EIS under dark as shown in Fig. S4. The lower charge transfer resistance of NR@TN is ascribed to the superior charge transport properties due to the interconnected thin nanosheets on the top of nanorods.

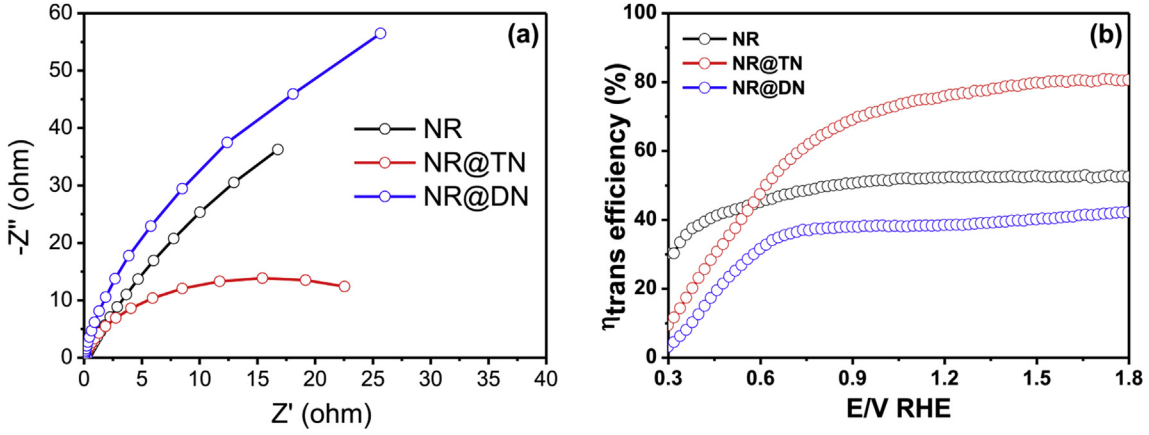

Fig. 8 – (a) Electrochemical impedance spectroscopy (EIS) of different photoelectrodes measured under illumination condition at open circuit voltage over a frequency range from 10^5 to 10^{-1} Hz with an AC voltage at 10 mV and (b) evaluation of charge transfer efficiency of various samples.

The EIS results were further supported by extracting charge transfer efficiency using hole scavenger method with Na_2SO_3 [50]. Fig. 8b shows the charge transfer efficiency of the fabricated ZnO photoanodes. The NR@TN structure showed superior charge transfer efficiency comparing to the other two ZnO photoanodes based on NR and NR@DN structures. The observed difference in charge transfer efficiency suggests that the thin nanosheets interconnected with nanorods provide more interfacial contact with electrolyte and thus effectively separate the charge carriers at photoanode/electrolyte interface. Compared to the NR@DN, however, the NR@TN has thin nanosheets which are very effective at transporting holes to the semiconductor/liquid interface for water oxidation as most electron/hole pairs are formed within a diffusion length of the semiconductor/liquid interface, ultimately minimizing recombination losses [51]. With a better absorption properties and faster charge transfer across the semiconductor–electrolyte interface, the NR@TN sample shows a higher PEC activity for water oxidation than NR and NR@DN samples.

As the solar water splitting is also an electrochemical phenomenon, the electrochemically active surface area (ECSA) is directly related to the PEC performance of photoanodes. The ECSA of each film was characterized from the capacitive region of cyclic voltammograms (CVs). Firstly, the double-layer charging region, −0.55 to −0.35, was determined from the representative CVs with the potential changed from −1 to +2 V vs. Ag/AgCl. The capacitive charging current density, i_c, was then measured from CVs in the capacitance range with a various of scan rate from 25 to 300 mV/s as shown in Fig. S5a. The i_c is equal to the scan rate, ν, multiply the electrochemical double-layer capacitance, C_{DL}, as given by $i_c = \nu C_{DL}$ [52]. The ECSA can be calculated from C_{DL} as ESCA $= C_{DL}/C_s$, where C_s is the intrinsic specific capacitance. Although the C_s can be exactly measured without an atomically flat ZnO reference standard, the relative electrochemical area can be determined by the ratio of the C_{DL} as shown in Fig. S5b. Although the NR@DN has highest specific surface area (as shown in Fig. 6), its value of ECSA is very low compared to NR and NR@TN. Due to the high specific surface made by the thin nanosheets, the ECSA of NR@TN is twice of NR. In addition, although NR doesn't have high specific surface area, it can efficiently utilize the interface between electrolyte and photoanode to separate the e–h pair so that it was observed a 1.2 times of ECSA compared to NR@DN. It indicates that the ESCA of photoanodes was not only dependent on the specific surface area of material but also determined by the structure.

The photoluminescence spectroscopy (PL) analysis of fabricated ZnO photoanodes was carried out to deeply understand the photoexcited electron transfer and electron–hole pair recombination process. As shown in Fig. 9, the prepared ZnO nanostructures were characterized by four main peaks, whose exact values were concluded in Table S1, accompanied by other small peaks. The PL peaks of Peak I are attributed to the transition near band edge [53]. The emission of Peak II is ascribed to the presence of zinc vacancy [54]. The Peak III situated at the same blue peak of 480 nm is associated to the transition between oxygen vacancy and interstitial oxygen [55]. Furthermore, the green emissions of Peak IV also were detected in all ZnO nanostructures. They could be attributed to recombination of electrons in singly occupied oxygen

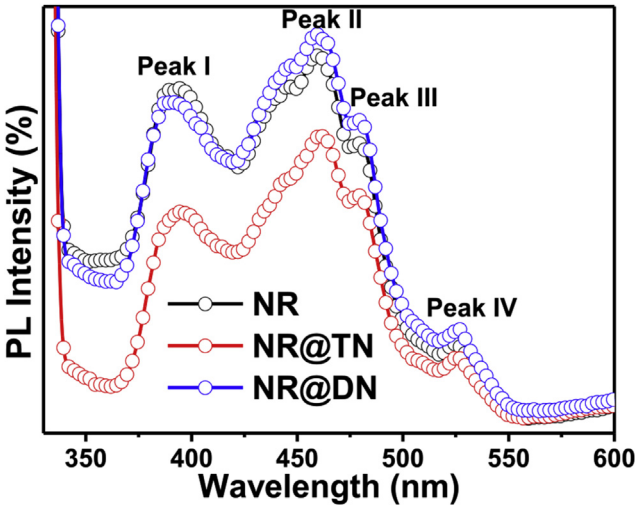

Fig. 9 – Photoluminescence spectroscopy analysis of as-prepared ZnO nanostructures such as nanorods (NR), nanorods interconnected by thin nanosheets (NR@TN) and nanorods interconnected by dense nanosheets (NR@DN).

vacancies with photoexcited holes [55] or the shallow donor levels of Zn_i^+ (charged zinc interstitial) to shallow acceptor levels of V_{Zn}^- (charged zinc vacancy). Overall, the intensity of PL spectra of NR@TN is much lower than NR, and NR@DN in the whole wavelength range. However, the intensities of the NR gradually become to lower than that of NR@DN after the Peak I and last continue to 600 nm. This PL spectra indicate that the NR@TN is much more beneficial to the carrier separation and has long lifetime of e–h pairs comparing to other two under light irradiation. In addition, the oxygen vacancies and defects play a significant role in the process of e–h pair fate, they act as an electron trap so that it is difficult for the electrons to go to the surface of electrode and recombine with holes. Therefore, the NR finally has better PEC performance than the NR@DN, although it has high e–h fair fate possibility near band edge.

On the basis of the above results, a tentative mechanism for enhanced PEC performance was proposed as illustrated in Scheme 1. Bright contrast was demonstrated through comparing with a traditional bulk geometries (left) which require high-quality materials such that the photogenerated minority-carrier diffusion length, L_{min}, is comparable to the characteristic light-absorption length, α^+. If electrons reach the interface between electrodes and electrolyte to generate hydrogen, most of them would be wiped out through recombining with holes. In contrast, the structured devices, such as NRAs (right), enable the orthogonalization of light absorption and carrier collection. Electrons are easy to arrive at the interface between electrodes and electrolyte directly across the transverse section of the NRAs. As a result, decoupling L_{min} from α^+ reduces certain materials quality constraints. In addition, the light can be transferred faster and enhance the light absorption due to the thin film on the top side of ZnO nanorods and its high roughness property. When the light irradiates the photoanode, some of light will be reflected, some of light will transmitted, however, greater amount of light will be transmitted and then repeatedly absorbed, scattered and reflected process until it wiped out by the thin nanosheets

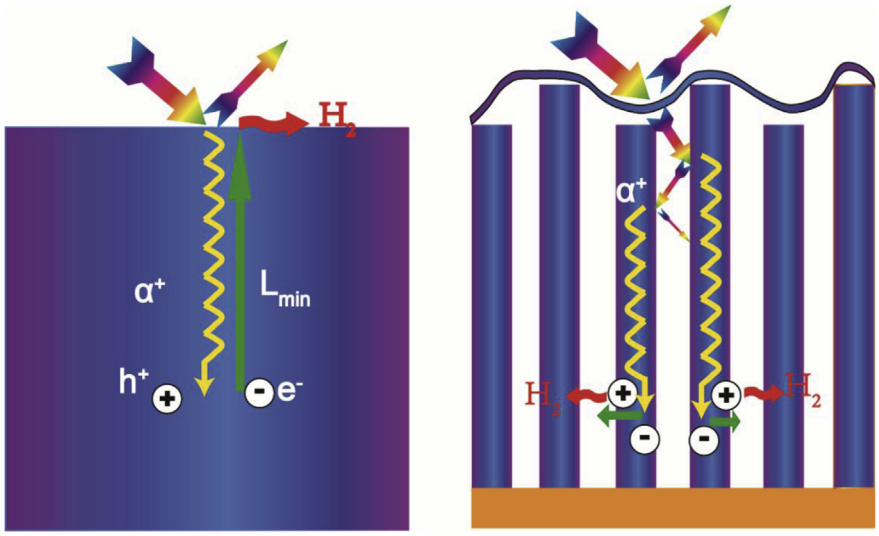

Scheme 1 – Schematic diagram of light trapping effect for enhanced light harvesting efficiency due to the NRAs interconnected by thin nanosheets architecture. Traditional bulk semiconductor geometries (left) require high-quality materials such that the photogenerated minority-carrier diffusion length, L_{min}, is comparable to the characteristic light-absorption length, α^{+}. In contrast, structured devices such as nanorod arrays (right) enable the orthogonalization of light absorption and carrier collection. Decoupling L_{min} from α^{+} reduces certain materials quality constraints. In addition, the light can be transferred longer distance to enhance the light absorption due to the thin film on the top side of ZnO nanorods and high surface roughness property.

interconnecting nanorods architecture. Nevertheless, less amount of optical would be absorbed when the top film is too thick. Because the light is difficult to penetrate into denser nanosheets less amounts of photons will be transferred through ZnO nanorods, which lead to less absorbance of light even comparing to pure nanorods. Finally, the NR@DN has lowest PEC performance comparing to NR and NR@TN.

Conclusions

Three types morphology of ZnO nanostructure films, vertically aligned nanorods, nanorods interconnected with thin nanosheets and nanorods interconnected by dense nanosheets, were prepared on the FTO glass plate with a facile hydrothermal method through controlling nanorods secondary growth time. The XRD, Micro-Raman and XPS analysis demonstrate that the as-prepared material is the hexagonal wurtzite crystal structured pure zinc oxide. The best PEC performance was obtained by NR@TN, which generated a photocurrent density of 0.62 mA/cm^2 at 1.23 V (vs. RHE) whereas the electrode based on NR and NR@DN produced the photocurrent of 0.5 mA/cm^2 and 0.45 mA/cm^2 at 1.23 V (vs. RHE) respectively. In addition, ~35% of enhanced optimal photoconversion efficiency was obtained at 0.77 V (vs. RHE) by NR@TN comparing to that of NR and NR@DN which demonstrate 0.135% and 0.13% at 0.82 V (vs. RHE). According to a series characterizations about optical properties, EIS and PL, the mechanism for enhanced PEC performance is noticeable: (i) special nanorods structure in which nanorods covered by very thin nanosheets at the tip, which is suitable for electrons transmission so that present ZnO nanorods have much better PEC performance than other reported work; and (ii) thin nanosheets, which is not only more effectively separate e–h pairs but also can capture more photons followed by being transferred to nanorods by making "light trapping", in comparison with NR, and vice versa for dense nanosheets. Undoubtedly, this work put forward a valuable theoretical thought to further improve the PEC performance of these ZnO photoanodes by combining this special structure with other technologies, such as doping, composite material, core–shell structure, and quantum dots.

Acknowledgements

This work was supported by National Research Foundation of Korea (NRF) grant funded by the Korea government (MSIP) (No. 2015R1A4A1041746). R. Boppella and D.H. Kim acknowledge the financial supported by National Research Foundation of Korea Grant funded by the Korean Government (No. 2014R1A2A1A09005656).

Appendix A. Supplementary data

Supplementary data related to this article can be found at http://dx.doi.org/10.1016/j.ijhydene.2017.04.121.

REFERENCES

[1] Hisatomi T, Kubota J, Domen K. Recent advances in semiconductors for photocatalytic and photoelectrochemical water splitting. Chem Soc Rev 2014;43:7520–35.

[2] Fujishima A. Electrochemical photolysis of water at a semiconductor electrode. Nature 1972;238:37–8.
[3] Boudjemaa A, Boumaza S, Trari M, Bouarab R, Bouguelia A. Physical and photo-electrochemical characterizations of α-Fe_2O_3. Application for hydrogen production. Int J Hydrogen Energy 2009;34:4268–74.
[4] Biswas SK, Baeg J-O. A facile one-step synthesis of single crystalline hierarchical WO_3 with enhanced activity for photoelectrochemical solar water oxidation. Int J Hydrogen Energy 2013;38:3177–88.
[5] Zhan F, Liu W, Li W, Li J, Yang Y, Li Y, et al. Efficient solar water oxidation by WO_3 plate arrays film decorated with CoO_x electrocatalyst. Int J Hydrogen Energy 2016;41:11925–32.
[6] Murcia-López S, Fàbrega C, Monllor-Satoca D, Hernández-Alonso MD, Penelas-Pérez G, Morata A, et al. Tailoring multilayered $BiVO_4$ photoanodes by pulsed laser deposition for water splitting. ACS Appl Mater Interf 2016;8:4076–85.
[7] Mu J, Chen B, Zhang M, Guo Z, Zhang P, Zhang Z, et al. Enhancement of the visible-light photocatalytic activity of In_2O_3–TiO_2 nanofiber heteroarchitectures. ACS Appl Mater Interf 2011;4:424–30.
[8] Meng M, Wu X, Zhu X, Yang L, Gan Z, Zhu X, et al. Cubic In_2O_3 microparticles for efficient photoelectrochemical oxygen evolution. J Phys Chem Lett 2014;5:4298–304.
[9] Qiu Y, Yan K, Deng H, Yang S. Secondary branching and nitrogen doping of ZnO nanotetrapods: building a highly active network for photoelectrochemical water splitting. Nano Lett 2011;12:407–13.
[10] Kochuveedu ST, Jang YH, Jang YJ, Kim DH. Visible light active photocatalysis on block copolymer induced strings of ZnO nanoparticles doped with carbon. J Mater Chem A 2013;1:898–905.
[11] Mao Y, Cheng Y, Wang J, Yang H, Li M, Chen J, et al. Amorphous NiO electrocatalyst overcoated ZnO nanorod photoanodes for enhanced photoelectrochemical performance. New J Chem 2016;40:107–12.
[12] Steinmiller EMP, Choi K-S. Photochemical deposition of cobalt-based oxygen evolving catalyst on a semiconductor photoanode for solar oxygen production. Acad Sci U S A 2009;106:20633–6.
[13] Miao J, Yang HB, Khoo SY, Liu B. Electrochemical fabrication of ZnO–CdSe core–shell nanorod arrays for efficient photoelectrochemical water splitting. Nanoscale 2013;5:11118–24.
[14] Chen HM, Chen CK, Lin CC, Liu R-S, Yang H, Chang W-S, et al. Multi-bandgap-sensitized ZnO nanorod photoelectrode arrays for water splitting: an X-ray absorption spectroscopy approach for the electronic evolution under solar illumination. J Phys Chem C 2011;115:21971–80.
[15] Liu Z, Wang Y, Wang B, Li Y, Liu Z, Han J, et al. PEC electrode of ZnO nanorods sensitized by CdS with different size and its photoelectric properties. Int J Hydrogen Energy 2013;38:10226–34.
[16] Lin C-J, Kao L-C, Huang Y, Bañares MA, Liou SY-H. Uniform deposition of coupled CdS and CdSe quantum dots on ZnO nanorod arrays as electrodes for photoelectrochemical solar water splitting. Int J Hydrogen Energy 2015;40:1388–93.
[17] Kushwaha A, Aslam M. ZnS shielded ZnO nanowire photoanodes for efficient water splitting. Electrochim Acta 2014;130:222–31.
[18] Liu M, Nam C-Y, Black CT, Kamcev J, Zhang L. Enhancing water splitting activity and chemical stability of zinc oxide nanowire photoanodes with ultrathin titania shells. J Phys Chem C 2013;117:13396–402.
[19] Shi M, Pan X, Qiu W, Zheng D, Xu M, Chen H. Si/ZnO core–shell nanowire arrays for photoelectrochemical water splitting. Int J Hydrogen Energy 2011;36:15153–9.
[20] Wang M, Ren F, Zhou J, Cai G, Cai L, Hu Y, et al. N doping to ZnO nanorods for photoelectrochemical water splitting under visible light: engineered impurity distribution and terraced band structure. Sci Rep 2015;5:12925.
[21] Cai L, Ren F, Wang M, Cai G, Chen Y, Liu Y, et al. V ions implanted ZnO nanorod arrays for photoelectrochemical water splitting under visible light. Int J Hydrogen Energy 2015;40:1394–401.
[22] Jiang J, Zhang X, Sun P, Zhang L. ZnO/BiOI heterostructures: photoinduced charge-transfer property and enhanced visible-light photocatalytic activity. J Phys Chem C 2011;115:20555–64.
[23] Wu M, Chen W-J, Shen Y-H, Huang F-Z, Li C-H, Li S-K. In situ growth of matchlike ZnO/Au plasmonic heterostructure for enhanced photoelectrochemical water splitting. ACS Appl Mater Interf 2014;6:15052–60.
[24] Feng W, Lin L, Li H, Chi B, Pu J, Li J. Hydrogenated TiO_2/ZnO heterojunction nanorod arrays with enhanced performance for photoelectrochemical water splitting. Int J Hydrogen Energy 2017;42:3938–46.
[25] McKone J, Lewis N. Structured materials for photoelectrochemical water splitting. In: Lewerenz H-J, Peter L, editors. Photoelectrochemical water splitting – materials, processes and architectures. Cambridge: RSC Publishing; 2013. p.52–82.
[26] Zhang X, Liu Y, Kang Z. 3D branched ZnO nanowire arrays decorated with plasmonic Au nanoparticles for high-performance photoelectrochemical water splitting. ACS Appl Mater Interf 2014;6:4480–9.
[27] Li Q, Sun X, Lozano K, Mao Y. Facile and scalable synthesis of "Caterpillar-like" ZnO nanostructures with enhanced photoelectrochemical water-splitting effect. J Phys Chem C 2014;118:13467–75.
[28] Emin S, Fanetti M, Abdi FF, Lisjak D, Valant M, van de Krol R, et al. Photoelectrochemical properties of cadmium chalcogenide-sensitized textured porous zinc oxide plate electrodes. ACS Appl Mater Interf 2013;5:1113–21.
[29] Fu M, Wang X, Zhao H, He D, Wang Y. Synthesis of ZnO inverse opals with high crystalline quality by a three-dimensional colloidal crystal template-assisted hydrothermal method over a seed layer. CrystEngComm 2016;18:7780–6.
[30] Cui X, Wang Y, Jiang G, Zhao Z, Xu C, Wei Y, et al. A photonic crystal-based CdS–Au–WO_3 heterostructure for efficient visible-light photocatalytic hydrogen and oxygen evolution. RSC Adv 2014;4:15689–94.
[31] Mitchell R, Brydson R, Douthwaite RE. Enhancement of hydrogen production using photoactive nanoparticles on a photochemically inert photonic macroporous support. Phys Chem Chem Phys 2015;17:493–9.
[32] Zhang P, Tachikawa T, Fujitsuka M, Majima T. Efficient charge separation on 3D architectures of TiO_2 mesocrystals packed with a chemically exfoliated MoS_2 shell in synergetic hydrogen evolution. Chem Commun 2015;51:7187–90.
[33] Vayssieres L, Keis K, Hagfeldt A, Lindquist S-E. Three-dimensional array of highly oriented crystalline ZnO microtubes. Chem Mater 2001;13:4395–8.
[34] Sounart TL, Liu J, Voigt JA, Hsu JWP, Spoerke ED, Tian Z, et al. Sequential nucleation and growth of complex nanostructured films. Adv Funct Mater 2006;16:335–44.
[35] Chen Z, Dinh HN, Miller E. Photoelectrochemical water splitting. New York: SpringerBriefs in Energy; 2013. p. 49–61.
[36] Kim H, Yong K. Highly efficient photoelectrochemical hydrogen generation using a quantum dot coupled hierarchical ZnO nanowires array. ACS Appl Mater Interf 2013;5:13258–64.
[37] Tian ZR, Voigt JA, Liu J, McKenzie B, McDermott MJ, Rodriguez MA, et al. Complex and oriented ZnO nanostructures. Nat Mater 2003;2:821–6.

[38] Cullity BD. Element of X-ray diffraction. Reading, MA: Addison-Wesley; 1978. p. 102. Google Scholar.
[39] Schumm M. ZnO-based semiconductors studied by Raman spectroscopy: semimagnetic alloying, doping and nanostructures. Suedwestdeutscher Verlag fuer Hochschulschriften 2010.
[40] Al-Gaashani R, Radiman S, Daud AR, Tabet N, Al-Douri Y. XPS and optical studies of different morphologies of ZnO nanostructures prepared by microwave methods. Ceram Int 2013;39:2283–92.
[41] Yang L-L, Zhao QX, Willander M, Liu XJ, Fahlman M, Yang JH. Origin of the surface recombination centers in ZnO nanorods arrays by X-ray photoelectron spectroscopy. Appl Surf Sci 2010;256:3592–7.
[42] Garnett E, Yang P. Light trapping in silicon nanowire solar cells. Nano Lett 2010;10:1082–7.
[43] Han SE, Chen G. Toward the Lambertian limit of light trapping in thin nanostructured silicon solar cells. Nano Lett 2010;10:4692–6.
[44] Yu Z, Raman A, Fan S. Fundamental limit of nanophotonic light trapping in solar cells. Proc Natl Acad Sci U S A 2010;107:17491–6.
[45] Wang X, Xiao Y, Zeng D, Xie C. Optimizing the packing density of TiO_2 nanorod arrays for enhanced light harvesting by a light trapping effect and its photocatalytic decomposition of gaseous benzene. CrystEngComm 2015;17:1151–8.
[46] Lowell S, Shields JE, Thomas MA, Thommes M. Characterization of porous solids and powders: surface area, pore size and density. Springer Science & Business Media; 2012.
[47] Thommes M, Kaneko K, Neimark AV, Olivier JP, Rodriguez-Reinoso F, Rouquerol J, et al. Physisorption of gases, with special reference to the evaluation of surface area and pore size distribution (IUPAC Technical Report). Pure Appl Chem 2015;87:1051–69.
[48] Peiris TAN, Sagu JS, Yusof YH, Wijayantha KGU. Microwave-assisted low temperature fabrication of ZnO thin film electrodes for solar energy harvesting. Thin Solid Films 2015;590:293–8.
[49] Zhang Z, Dua R, Zhang L, Zhu H, Zhang H, Wang P. Carbon-layer-protected cuprous oxide nanowire arrays for efficient water reduction. Acs Nano 2013;7:1709–17.
[50] Kim TW, Choi K-S. Nanoporous $BiVO_4$ photoanodes with dual-layer oxygen evolution catalysts for solar water splitting. Science 2014;343:990–4.
[51] Cho IS, Chen Z, Forman AJ, Kim DR, Rao PM, Jaramillo TF, et al. Branched TiO_2 nanorods for photoelectrochemical hydrogen production. Nano Lett 2011;11:4978–84.
[52] Feng X, Chen Y, Qin Z, Wang M, Guo L. Facile fabrication of sandwich structured WO_3 nanoplate arrays for efficient photoelectrochemical water splitting. ACS Appl Mater Interf 2016;8:18089–96.
[53] Zeng H, Duan G, Li Y, Yang S, Xu X, Cai W. Blue Luminescence of ZnO nanoparticles based on non-equilibrium processes: defect origins and emission controls. Adv Funct Mater 2010;20:561–72.
[54] Tam KH, Cheung CK, Leung YH, Djurišic AB, Ling CC, Beling CD, et al. Defects in ZnO nanorods prepared by a hydrothermal method. J Phys Chem B 2006;110:20865–71.
[55] Boukos N, Chandrinou C, Giannakopoulos K, Pistolis G, Travlos A. Growth of ZnO nanorods by a simple chemical method. Appl Phys A Mater Sci Process 2007;88:35–9.